

## ARTICLE

## OPEN



# Decoherence of nitrogen-vacancy spin ensembles in a nitrogen electron-nuclear spin bath in diamond

Huijin Park<sup>1,5</sup>, Junghyun Lee<sup>2,5</sup>, Sangwook Han<sup>1,2,3</sup>, Sangwon Oh<sup>4</sup>✉ and Hosung Seo<sup>1</sup>✉

Nitrogen-vacancy (NV) centers in diamond have been developed into essential hardware units for a wide range of solid-state-based quantum technology applications. While such applications require the long spin coherence times of the NV centers, they are often limited due to decoherence. In this study, we theoretically investigate the decoherence of NV-spin ensembles induced by nitrogen impurities (P1 centers), which are one of the most dominant and inevitable magnetic field noise sources in diamond. We combined cluster correlation expansion and density functional theory to compute the Hahn-echo spin-coherence time of the NV centers for a broad range of P1 concentrations. Results indicate a clear linear dependence of  $T_2$  on P1 concentrations on a log scale with a slope of  $-1.06$ , which is in excellent agreement with previous experimental results. The interplay between the Jahn-Teller effect and the hyperfine interaction in the P1 center plays a critical role in determining the bath dynamics and the resulting NV decoherence. Our results provide a theoretical upper bound for the NV-spin  $T_2$  over a wide range of P1 densities, serving as a key reference for materials optimization and spin bath characterization to develop highly coherent NV-based devices for quantum information technology.

*npj Quantum Information* (2022)8:95 ; <https://doi.org/10.1038/s41534-022-00605-4>

## INTRODUCTION

Nitrogen-vacancy (NV) centers in diamond are one of the leading solid-state-based qubit platforms, enabling diverse quantum applications including quantum information processing<sup>1–4</sup>, quantum sensing<sup>5–8</sup>, and quantum networks<sup>9,10</sup>. For a spin qubit, a long spin coherence time is one of the key properties that an NV center should possess because it plays a critical role in determining the performance of a spin qubit in quantum applications<sup>6</sup>. Combined with spin bath decoupling methods or bath engineering techniques, the Hahn-echo spin-coherence time ( $T_2$ ) of an NV center has been shown to reach  $\sim 1$  s<sup>11–13</sup>. In practical applications, however, the spin coherence time of an NV center could be significantly degraded due to intensified decoherence caused by paramagnetic spin defects<sup>14</sup>, which in turn could limit the range of NV-spin qubit-based quantum applications<sup>14,15</sup>.

NV-spin decoherence has been extensively investigated and the dominant mechanism has been found to involve the coupling of the NV-spin dipolar to the fluctuating spin bath in diamond<sup>16</sup>. Two dominant types of spin baths identified are those with <sup>13</sup>C nuclear spins (natural abundance 1.1%,  $I = 1/2$ ) and those considered as electronic spin baths with substitutional nitrogen electron-nuclear spins (the so-called P1 bath, <sup>14</sup>N 99.6%,  $S = 1/2$ , and  $I = 1$ ). In a 1.1% <sup>13</sup>C nuclear-spin-dominant bath, the NV-spin's Hahn-echo coherence time ( $T_2$ ) has been reported to be larger than 600  $\mu$ s<sup>17–19</sup> and its decoherence dynamics is theoretically well understood<sup>20</sup>. Building upon this established knowledge, several methods have also been developed to suppress the <sup>13</sup>C-induced decoherence of the NV spin, including a dynamical decoupling method<sup>21</sup> and <sup>12</sup>C isotopic purification of a diamond sample<sup>18</sup>. Meanwhile, it is well known that the paramagnetic spins in diamond, or P1 centers<sup>22</sup>, are one of the dominant sources of NV-spin decoherence<sup>23–27</sup>. It has been shown that the NV-spin coherence is much more fragile under the presence of P1 spins

than in a <sup>13</sup>C nuclear-spin bath owing to the larger gyromagnetic ratio of P1 spins<sup>24,25,27,28</sup>. Nevertheless, P1-induced NV-spin decoherence is less understood than <sup>13</sup>C-induced decoherence.

Recently, understanding the NV-spin decoherence mechanism due to various P1 concentrations ([P1]) has gained much interest<sup>29–34</sup> in several important applications such as nuclear-spin hyperpolarization<sup>35</sup>, quantum sensing<sup>5,6</sup>, and quantum information applications<sup>1,36,37</sup>. Such applications may require either high NV densities or the controlled creation of P1 centers. In the NV center generation process, however, P1 centers are inevitably created with different concentrations (1–100 ppm) owing to the low N-to-NV center yield rate (<25%)<sup>35,38</sup>, which, in turn, may lead to the degraded coherence of the NV center due to the P1 centers<sup>7</sup>. Thus, it is of paramount importance to systematically understand P1-induced NV decoherence as a function of [P1].

Recent studies have made significant progress towards the quantitative analysis of P1-induced NV-spin decoherence. In particular, it has become possible to determine [P1] in a diamond sample with high precision<sup>30,31</sup>, enabling measurements of the NV's  $T_2$  as a function of [P1]<sup>29–32</sup>. Recently, Bauch et al.<sup>29</sup> reported the  $T_2$  of an NV-spin ensemble as a function of [P1], showing a linear dependence of  $T_2$  on [P1] on a log scale with a stretched exponential parameter ( $n$ ) of  $\sim 1.37$ , which describes the exponential decay of the NV coherence as  $\exp\left(-\left(\frac{t}{T_2}\right)^n\right)$ . In another recent work by Li et al.<sup>30</sup> a local spin bath measurement technique is developed to extract the position-dependent concentration of various paramagnetic defects in a diamond sample. Importantly, however, the linear dependence between  $T_2$  and [P1] found in the semi-classical simulation of the previous study<sup>29</sup> was much less clear. In addition, the stretching exponent measured varied significantly depending on [P1], which also deviates from that of the previous result<sup>29</sup>. Li et al.<sup>30</sup> and

<sup>1</sup>Department of Physics and Department of Energy Systems Research, Ajou University, Suwon, Gyeonggi, Republic of Korea. <sup>2</sup>Center for Quantum Information, Korea Institute of Science and Technology, Seoul, Republic of Korea. <sup>3</sup>Division of Nano and Information Technology, KIST School, Korea University of Science and Technology, Seoul, Korea. <sup>4</sup>Korean Research Institute of Standards and Science, Daejeon, Republic of Korea. <sup>5</sup>These authors contributed equally: Huijin Park, Junghyun Lee. ✉email: sangwon.oh@kriss.re.kr; hseo2017@ajou.ac.kr

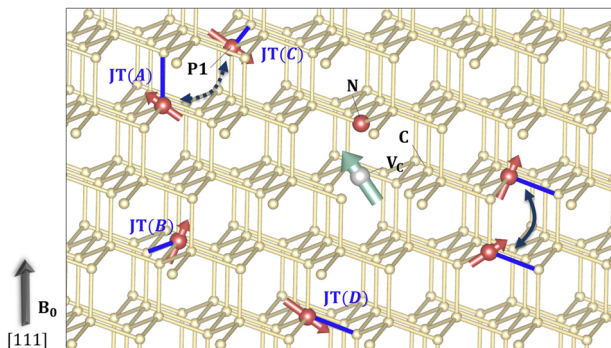


**Fig. 1 Diamond NV center in a P1 bath.** Schematic of a nitrogen-vacancy (NV) electron spin (green arrow) surrounded by substitutional nitrogen impurities (P1 centers). The direction of the NV center is parallel to the external magnetic field  $B_0$ , which points in the [111] direction. The NV center spin interacts with the P1 spins (red arrow), which includes both an electron spin ( $S = 1/2$ ) and nuclear spin ( $I = 1$ ) via a magnetic dipole-dipole interaction. A P1 center can have one of four different Jahn–Teller axes denoted as JT(A), JT(B), JT(C), and JT(D), which are represented by a blue bar for each P1 center.

other researchers have suggested that the deviation may be caused by extra paramagnetic defects other than the P1 centers in the sample.

The lack of a full understanding of the NV's  $T_2$  vs. [P1] and the role of extra electronic spins can benefit from the accurate theoretical prediction of  $T_2$ ([P1]), which can provide an upper bound for  $T_2$  and a reference for the stretched exponential parameter of a P1-dominant bath. Early theoretical studies have shown that the basic property of P1-induced NV-spin decoherence can be analyzed by using semi-classical theories based on the Ornstein–Uhlenbeck (O-U) process. Notably, a similar semi-classical method was used to understand recent experimental measurements<sup>29,30</sup>, and the overall qualitative tendency of  $T_2$  as a function of [P1] was reproduced. The semi-classical results, however, underestimate the  $T_2$  and overestimate the slope over a wide range of P1 concentrations<sup>29</sup>. In this regard, first-principles calculations with a predictive power are necessary to provide a quantitative theoretical guidance to P1-induced NV decoherence.

In this study, we perform fully quantum mechanical calculations by combining cluster correlation expansion and density functional theory (DFT) to investigate the P1-induced decoherence dynamics of a negatively charged NV ensemble for a broad range of [P1]. We compute the Hahn-echo  $T_2$  as a function of [P1] and our results provide a theoretical upper bound for  $T_2$  from 1 to 100 ppm. We show that the  $T_2$ ([P1]) exhibits a clear linear dependence on a log scale with a slope of  $-1.06$ , which is in excellent agreement with the experimental result of  $-1.07^{29,31}$ . We found that the stretched exponential parameter is close to 1 for the [P1] from 1 to 100 ppm. Building upon these results, we show that the Jahn–Teller-derived anisotropy in the hyperfine interaction of the P1 center plays a crucial role in determining P1 bath dynamics. Our study offers a complete understanding of the P1-induced spin decoherence dynamics of an NV ensemble, which can provide a key reference for developing diamond samples with optimized NV-spin coherence for different applications.

## RESULTS

### System and model

We adopt a central spin model to compute the decoherence dynamics of an NV-spin interacting with a substitutional nitrogen impurity spin bath. We use the Hahn-echo pulse sequence, which has a  $\pi$  pulse in between two free evolution time periods  $\tau$  to compute the homogeneous dephasing time  $T_2$

of NV-spin ensembles<sup>39,40</sup>. The degree of NV-spin decoherence is obtained by computing the off-diagonal element of the reduced density matrix of the NV spin after tracing out the bath degrees of freedom at the end of the  $2\tau$  free evolution time<sup>39</sup> (see Methods for details).

Figure 1 shows our central spin model in detail. The NV center is a spin-1 electronic defect, which consists of a C vacancy and substitutional N atom paired along the [111] crystal direction. The P1 center is an isolated substitutional nitrogen impurity that replaces a carbon atom in the diamond lattice. In our model, P1 spins are randomly distributed around the NV spins. We consider various [P1] from 1 ppm to 100 ppm, which are commonly found in diamond samples used in magnetometry and quantum simulation applications<sup>29,34,36,41–44</sup>. An NV spin is coupled to the P1 centers via the magnetic dipole–dipole interaction (see Supplementary Note 1). To compute the maximum  $T_2$  time of the NV ensembles imposed by the P1 bath, we applied an external magnetic field of 500 G in the same direction as the symmetry axis of the NV spin, over which the NV decoherence is mainly driven by flip-flop transitions between P1 spins. We note that the cross-relaxation effect between the NV and P1 spins, which occurs near  $B = 514$  G<sup>45,46</sup> was not included. The P1 center accompanies an electron spin-1/2 and a nuclear spins-1 (spin-1/2) for  $^{14}\text{N}$  ( $^{15}\text{N}$ , natural abundance of 0.37%), which are strongly coupled to each other via a hyperfine interaction (see Supplementary Note 2). The electronic spin of the P1 center is highly localized at the lattice site due to the Jahn–Teller (JT) effect<sup>47</sup>.

The JT effect creates strong anisotropy in the hyperfine interaction of the P1 center<sup>48,49</sup> and induces a strong lattice relaxation in such a way that the N atom is distorted away from one of the four nearest neighboring C atoms, leading to four possible hyperfine anisotropy axes. In Supplementary Information, we provide a detailed description of the anisotropic hyperfine tensors. We compared our density functional theory (DFT) calculations with experimental results<sup>37</sup>, the comparison of which demonstrated excellent agreement for the four different hyperfine anisotropy axes (see Supplementary Note 2). In our central spin model (see Fig. 1), the four possible anisotropy axes are randomly assigned to the P1 centers. In addition, the given anisotropy axis for the P1 centers is fixed during the simulation as the time scale of the JT axis change is known to be from  $10^3$  to  $10^5$  s in low temperatures ( $\leq 200$  K)<sup>50</sup>, which is much larger than the time scale of NV-spin decoherence, which is in the order of hundreds of microseconds.

To compute the NV-spin's  $T_2$  induced by a large number of P1 centers, we employ the cluster correlation expansion method (CCE)<sup>39,40,51</sup>, which enables a predictive quantum mechanical computation of  $T_2$  without assuming any adjustable theoretical parameters. The CCE method was successfully applied to a wide range of central spin models including both nuclear<sup>20,52,53</sup> and electron spin baths<sup>54,55</sup>, yielding an excellent agreement with experimental results<sup>53,55</sup>. Further details on the spin Hamiltonian, theoretical methods, and the numerical convergence tests can be found in the Methods section and Supplementary Notes 3 and 4.

It is worth noting that our NV decoherence model do not include the spin-lattice relaxation ( $T_1$ ) effects of the P1 center<sup>27,56</sup> and the NV center<sup>27,45</sup>, which may be a valid assumption to model the P1-driven NV decoherence at room temperature. At room temperature and below, the  $T_1$  time of the P1 center is longer than ms, meaning that thermally driven random flips of the P1 spins are unlikely in the time scale of the NV spin echo decoherence. We note, however, that the spin-lattice relaxation could significantly contribute to the NV decoherence if temperature is much higher than the room temperature as the  $T_1$  time of the P1 center significantly decreases as the temperature increases<sup>27,45,56</sup>.

### The coherence time of the NV center as a function of [P1]

Figure 2 presents the computed Hahn-echo  $T_2$  of NV ensembles in a P1 bath as a function of [P1] from 1 to 100 ppm. The computed  $T_2$  time was compared with previous experimental results<sup>29–31</sup>. Our findings indicate that the computed  $T_2$  time provides a proper upper bound for the spin-coherence time of the NV ensemble in the P1 environment. In Fig. 2, it can be observed that the theoretical results are consistently 2–4 times larger than the experimental results: the theoretical (experimental)  $T_2$  times are 98.2  $\mu$ s (40  $\mu$ s), 18.4  $\mu$ s (5  $\mu$ s), and 8.4  $\mu$ s (2  $\mu$ s) at 4 ppm, 20 ppm, and 40 ppm, respectively. Furthermore, the

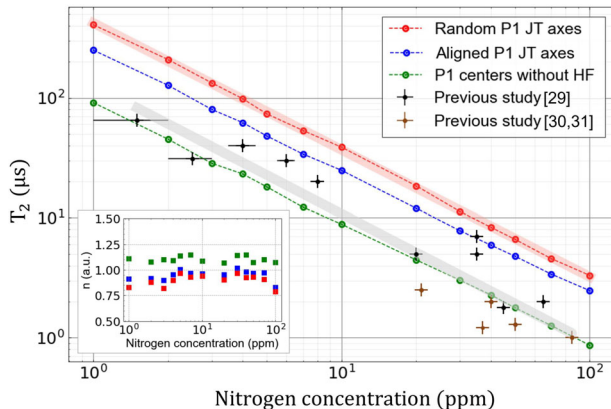


**Fig. 2 Coherence times of diamond NV ensembles in a P1 bath.** Hahn-echo coherence times ( $T_2$ ) as a function of [P1] with random P1 JT axes (red dots) compared with previous experimental data of  $T_2$  (black<sup>29</sup> and brown<sup>30,31</sup> crosses). An external magnetic field of 500 G was applied along the [111] direction for the computation. Two hypothetical P1 bath models were considered: a P1 bath in which all the JT axes are polarized in the [111] direction (blue dots) and a P1 bath in which the P1 hyperfine interaction is ignored (green dots). The gray shaded line is the fitted line for the experimental data to be compared with the red shaded line, which is the fitted line for our computational results. Inset: stretched exponential parameters ( $n$ ) for the P1 bath models with no-hyperfine interaction (green marker), polarized P1 JT axes (blue marker), and randomized P1 JT axes (red marker).

theoretical  $T_2$  time shows a clear linear dependence on [P1] on a log scale with a slope of  $-1.06$ , which is in excellent agreement with the previous experimental observations<sup>29–31</sup> that present a slope of  $-1.07$  on a log scale.

In terms of the stretching exponent ( $n$ ) of the NV-spin's coherence decay curve,  $n$  increases slowly as a function of [P1] and the average value is found to be 0.9 as shown in Fig. 2. The  $n$  values are  $\sim 0.8$  and  $\sim 0.9$  at low [P1] around 3 ppm and at high [P1] around 50 ppm, respectively. The CCE results are reasonably consistent with recent experimental measurements, which yielded  $n = 1.37 \pm 0.23$ <sup>29</sup>. It is worth noting that O–U based semi-classical theory predictions of  $n$  could vary from 1 (motional-narrowing regime) to 3 (quasi-static regime)<sup>29,33</sup>. Several early experimental studies reported scattered results for  $n$  from 1 to 3<sup>26,31,33</sup>. For the NV-spin ensemble in a pure P1 bath, our CCE calculations show that the shape of the NV's spin-echo decay curve is close to the curve of a single exponential function.

The large deviation of the experimental  $T_2$  results from the theoretical calculations obtained for a pure P1 bath indicates the important potential role of parasitic electron spins in addition to P1 centers that act as extra decoherence sources<sup>30,34,57,58</sup>. In Fig. 3, the effect of adding extra electronic spins ( $S = 1/2$  with  $g = 2$ ) in a P1 bath is examined<sup>30</sup> (see Supplementary Note 5). Interestingly, our results indicate that the experimental  $T_2$  time can be reproduced in theory when the concentration of the extra spins ([Ex]) is similar to [P1], which indicates a close relationship between [Ex] and [P1]. Figure 3a, b show the computed NV's spin coherence for [P1] = 1 ppm and 5 ppm, respectively, by varying [Ex] from 0 to 6 ppm. It can be observed that the NV's spin coherence is highly sensitive to the presence of extra spins, and  $T_2$  and  $n$  significantly change as [Ex] increases. When [Ex] is 2 ppm (see Fig. 3c, d), the computed  $T_2$  for [P1] = 1 ppm is 60.7  $\mu$ s, which matches well with the experimental  $T_2$  time of 65  $\mu$ s.  $n$  is computed to be  $\sim 0.74$  and  $\sim 0.92$  for [Ex] = 0 ppm and 2 ppm, respectively. For a P1 spin bath with [P1] = 5 ppm (see Fig. 3e, f), the experimentally measured  $T_2$  time of  $\sim 30$   $\mu$ s is theoretically reproduced when [Ex] is 5 ppm, yielding  $T_2 = 28.2$   $\mu$ s. The same trend holds for a P1 bath with [P1] = 12 ppm and [P1] = 50 ppm as shown in Supplementary Fig. 5. Our results suggest the importance of considering extra electronic spins and their potential correlation with the P1 centers to describe the NV-spin decoherence dynamics more accurately in a P1 bath.

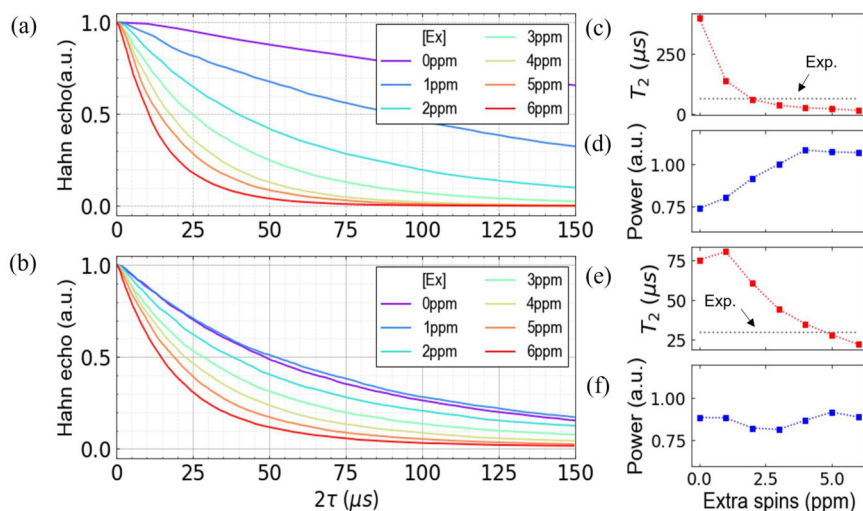


**Fig. 3 NV decoherence in a P1 bath with extra electron spins.** **a, b** Computed Hahn-echo coherence of NV ensembles for [P1] = 1 ppm (a) and 5 ppm (b) with varying extra spin concentrations ([Ex]) from 0 to 6 ppm. **c, d**  $T_2$  times (c) and stretched exponential parameter (d) of the NV coherence as a function of [Ex] for [P1] = 1 ppm. **e, f**  $T_2$  times (e) and stretched exponential parameter (f) of the NV coherence as a function of [Ex] for [P1] = 5 ppm. In (c, e), the black dotted line shows an experimental  $T_2$  time of 65  $\mu$ s and 30  $\mu$ s for [P1] = 1.5 ppm and 6 ppm, respectively, taken from the reference<sup>29</sup>.

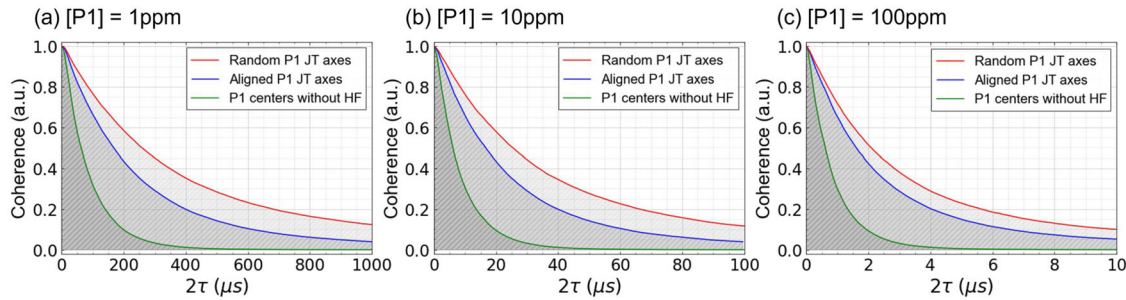


**Fig. 4 Spin coherence of NV ensembles in a P1 bath.** **a–c** Hahn-echo coherence of NV ensembles (red line) for  $[P1] = 1$  ppm (a), 10 ppm (b), and 100 ppm (c) compared with the coherence function obtained with two hypothetical P1 bath models: P1 bath with no-hyperfine interaction (green line) and a P1 bath in which all the JT axes are polarized along the (111) direction (blue line).

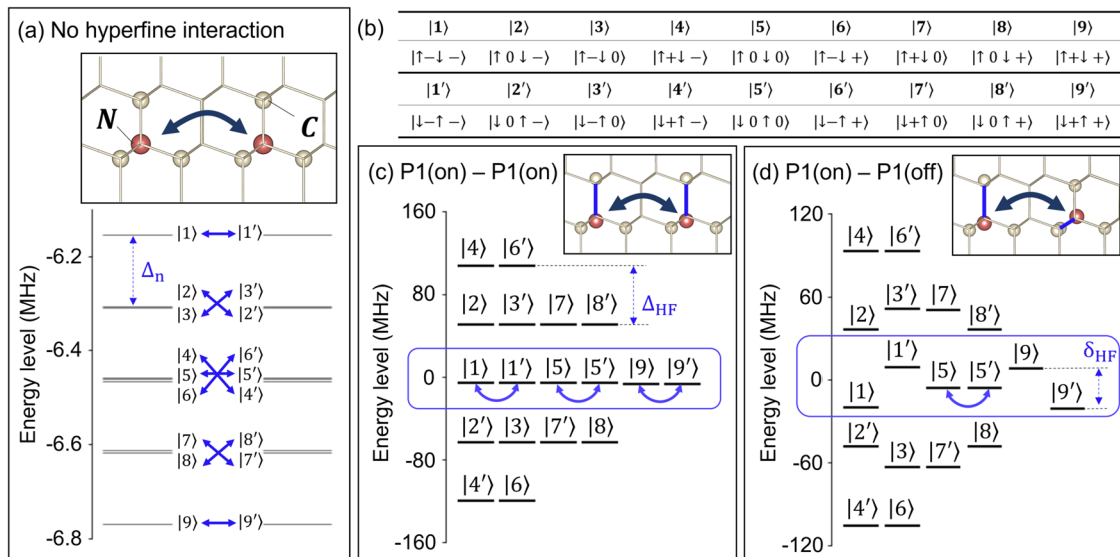


**Fig. 5 Energy levels of a P1-P1 pair.** **a** Energy level diagram of two P1 centers in which the on-site hyperfine interaction is ignored. The upper panel represents two P1 centers interacting with each other. The energy level diagram only shows states derived from  $|\uparrow_1\downarrow_2\rangle$  and  $|\downarrow_1\uparrow_2\rangle$ , where  $|\uparrow\rangle$  and  $|\downarrow\rangle$  are the  $m_s = +1/2$  and  $-1/2$  states of the P1 electron spin, respectively. Considering the nuclear-spin states ( $|+\rangle$  for  $m_i = 1, |0\rangle$  for  $m_i = 0$ , and  $|-rangle$  for  $m_i = -1$ ), there are 18 states, which are labeled as  $|1\rangle, \dots, |9\rangle$  for the  $|\uparrow_1\downarrow_2\rangle$ -derived states, and  $|1', \dots, |9'\rangle$  for the  $|\downarrow_1\uparrow_2\rangle$ -derived states as specified in (b). In the absence of the hyperfine interaction (a), the spin states are split by nuclear Zeeman splitting ( $\Delta_n$ ) and 9 electron spin flip-flop transition channels are allowed (indicated by blue arrows). **c** Energy levels of a P1 pair having the same JT axes parallel to the [111] direction. The energy levels are largely shifted by the hyperfine interaction on the order of tens of MHz ( $\Delta_{HF}$ ). The electron spin flip-flop transitions are allowed only between  $|1\rangle \leftrightarrow |1'\rangle$ ,  $|5\rangle \leftrightarrow |5'\rangle$  and  $|9\rangle \leftrightarrow |9'\rangle$  due to the energy level shifts. **d** Similar energy level diagram for a P1 pair whose JT axes are not parallel (see inset). The energy levels are further split by the difference in the hyperfine interactions ( $\delta_{HF}$ ). The electron spin flip-flop transition is only allowed between  $|5\rangle \leftrightarrow |5'\rangle$ .

### The role of $^{14}\text{N}$ nuclear spin in the P1-P1 flip-flop dynamics

To better understand P1-induced NV-spin decoherence, the P1 bath dynamics were analyzed with a focus on the role of the N nuclear spin in controlling the flip-flop dynamics between the P1 electron spins. It is worth mentioning that the nuclear-spin flip-flop dynamics can be safely ignored because its time scale is much longer than those of the electron spin flip-flop transition rate and NV decoherence. With the electron spin flip-flop transition as the dominant source of magnetic field noise from the bath, fast flip-flop transitions imply fast NV-spin coherence decays. In what follows, we show that the P1 electron spin flip-flop transitions are significantly suppressed by the hyperfine interaction of the P1 center and JT-derived anisotropy in the hyperfine interaction.

Figure 4 compares the NV-spin coherence computed for a pure P1 bath, whose JT axes are random, with two hypothetical P1 bath models for  $[P1] = 1, 10$ , and  $100$  ppm: the P1 centers with no-hyperfine interaction and the P1 centers whose JT axes are all fixed in one direction. The P1 spin bath with no-hyperfine interaction is effectively the same as a bare electron spin bath in the time scale of a few hundreds of microseconds because the slow N nuclear-spin

bath is decoupled from the electron spins. As shown in Fig. 4, the NV coherence in such “no-hyperfine” P1 bath model quickly decays due to the flip-flop transitions between the bare electron spins, yielding  $T_2$  times of  $91.15\ \mu\text{s}$ ,  $8.85\ \mu\text{s}$ , and  $0.87\ \mu\text{s}$  for  $[P1] = 1, 10$ , and  $100$  ppm, respectively. Interestingly, however, we observed that the NV’s coherence is significantly enhanced when we include the hyperfine interaction between the electron and nuclear spins of the P1 center. For  $[P1] = 1, 10$ , and  $100$  ppm, the  $T_2$  times are increased to  $249.62\ \mu\text{s}$ ,  $24.83\ \mu\text{s}$ , and  $2.47\ \mu\text{s}$ , respectively, when the JT axes are fixed to one direction. The  $T_2$  times are further increased to  $406.61\ \mu\text{s}$ ,  $38.73\ \mu\text{s}$ , and  $3.32\ \mu\text{s}$  for  $[P1] = 1, 10$ , and  $100$  ppm, respectively, when the JT axes in the P1 bath are randomized. In addition to the P1 concentrations considered in Fig. 4, we also compared the  $T_2$  times computed using the three bath models for other  $[P1]$  from  $1$  ppm to  $100$  ppm, the results of which are reported in Fig. 2 and from which the same conclusions are drawn. Our calculation results show that the electron spin flip-flop dynamics are significantly suppressed in the presence of the N nuclear spin due to the hyperfine interaction and JT-induced anisotropy in the hyperfine interaction.

To elucidate the hyperfine-induced suppression of the P1 electron spin flip-flop dynamics, we analyzed the energy levels of a P1-P1 spin pair for the three P1 bath models in Fig. 5. Figure 5a shows the energy levels in the absence of the hyperfine interaction. We only considered the states whose electron spins are up and down ( $|\uparrow\downarrow\rangle$  or  $|\downarrow\uparrow\rangle$ ) because they are coupled by the electron spin dipolar flip-flop interaction. Considering the nuclear-spin state ( $|+\rangle$ ,  $|0\rangle$ ,  $|-\rangle$ ), there are 18 possible states whose electron spins are up and down as listed in Fig. 5b. In the absence of the hyperfine interaction, there are 9 active flip-flop transition channels as shown in Fig. 5a due to the nuclear Zeeman energy splitting ( $\Delta_n \sim 154$  kHz) and the mismatch in the nuclear-spin states (i.e.,  $|\uparrow\downarrow 0\rangle \leftrightarrow |\downarrow\uparrow 0\rangle$  is allowed,  $|\uparrow\downarrow -\rangle \leftrightarrow |\downarrow\uparrow -\rangle$  is not allowed). However, when the hyperfine interaction is turned on in the bath, the number of these flip-flop channels is greatly reduced. For two P1 centers having the same JT axes, the number of flip-flop channels is three due to the energy level mismatch induced by the hyperfine interaction ( $\Delta_{HF} \approx \frac{1}{2}A_{||}^{on} \approx 57$  MHz). In addition, for a P1-P1 pair with different JT axes, the degenerated states obtain an additional energy shift ( $\delta_{HF} \approx A_{||} - A'_{||} \approx 29$  MHz), which reduces the number of flip-flop channels to only one. Our results show that the electron spin flip-flop transitions are largely suppressed in the presence of the JT-derived anisotropic hyperfine interaction.

## DISCUSSION

We performed full quantum calculations of the  $T_2$  time of diamond NV-spin ensembles in a P1 spin bath with the function of the P1 concentration varying from 1 ppm to 100 ppm by combining DFT and cluster correlation expansion. Our results show a clear linear dependence of the  $T_2$  time on [P1] on a log scale with a slope of  $-1.06$ , which is consistent with a slope of  $-1.07$  used to describe  $T_2$  vs [P1] in the log scale in the previous study<sup>29</sup>. By systematically analyzing three different P1 spin bath models, we have found that the electron spin flip-flop dynamics in a P1 bath are largely suppressed in the presence of the anisotropic P1 hyperfine interaction. It is shown that the N nuclear spin induces various shifts in the P1 energy levels on the order of hundreds of MHz through hyperfine coupling, suppressing the electron spin flip-flop transitions.

It is worth commenting that the relation between  $T_2$  and  $[N_s^0]$  derived in this study could be applied to estimate the P1 concentration and the N to NV<sup>-</sup> conversion ratio, which are crucial information in NV-based magnetometry and quantum simulation applications since varying [P1] can vastly change the ensemble spin dynamics. Our result shows that  $T_2 = 416.65 \times [P1]^{-1.06}$   $\mu$ s for  $[P1] > 1$  ppm, assuming the P1 spins to be the dominant spin bath. By relating measured  $T_2$  to the CCE derived relation, one can extract the lower-bound for [P1] without any destructive measurements. In addition, the sensitivity of echo-based AC magnetometry can be expressed as<sup>7</sup>  $\eta \propto \frac{1}{\sqrt{NT_2}} \cdot \sqrt{\frac{T_2 + \tau_i + \tau_R}{T_2}}$ , where  $N$  is the total number of sensor spins,  $T_2$  is the Hahn echo spin coherence time,  $\tau_i$  is the initialization time, and  $\tau_R$  is the readout time. Typical values for  $\tau_i + \tau_R \sim 5$   $\mu$ s for NV ensemble sensor. Since  $N \propto [NV^-] = c \cdot [P1]$ , where  $c$  is the [P1] to [NV<sup>-</sup>] conversion ratio, the sensitivity as a function of [P1] can be simplified as  $\eta \propto \sqrt{[P1]/c}$ . By measuring NV ensemble sensor's echo AC magnetometer noise floor and relating that to estimated [P1], one can calculate the conversion ratio  $c$ .

Additionally, the computed  $T_2$  times are consistently larger than previous experimental results, which indicates the importance of other decoherence sources in describing the NV-spin decoherence in a P1 spin bath. In our study, we considered extra electron spins as an additional source of decoherence inspired by recent studies<sup>30</sup>. Notably, we found that the calculated  $T_2$  time becomes

similar to the experimental  $T_2$  time when the concentration of the extra spins is similar to the P1 concentration, which may indicate a close relationship between the concentration of extra parasitic spins and the P1 concentration in diamond.

It should be noted, however, that other paramagnetic defects or complexes could be considered as possible extra spins to better understand the source of the NV decoherence<sup>58</sup>. During the CVD growth or ion-implantation to create NV centers in diamond, many vacancies or defect complexes could be easily formed, acting as parasitic spins in the diamond lattice. Such examples may include NV<sup>0</sup> ( $S = 1/2$ ), NVH<sup>-</sup> ( $S = 1/2$ ), VH<sup>0</sup> ( $S = 1/2$ ), VH<sup>-</sup> ( $S = 1$ ), N<sub>2</sub><sup>+</sup> ( $S = 1/2$ ), V<sup>-</sup> ( $S = 3/2$ ), V<sup>+</sup> ( $S = 1/2$ ), WV<sup>0</sup> ( $S = 1$ ), to name a few, which are paramagnetic defects commonly found in diamond<sup>7</sup>. However, their contribution to the NV decoherence is largely unknown. We remark that the methods developed in this work could be applied to study these defects, which we planned as a separate future study. Further systematic investigation on other paramagnetic spins will help to better understand NV-spin decoherence in practical applications.

Electron dipolar spin ensembles in diamond are already being exploited for practical applications such as quantum sensing or quantum simulations. Understanding the bath spin ensemble dynamics derived from the results obtained in our study could be a vital resource in the engineering of NV-spin-based scalable quantum systems for quantum-enhanced technologies.

## METHODS

### Cluster correlation expansion computation

To compute the  $T_2$  time of diamond NV ensembles, we implemented the single-sample CCE theory in our in-house CCE code, and several important features of our CCE computation can be summarized as follows. The P1 bath was clustered in terms of the number of P1 centers instead of the number of spins in the original CCE formulation. For example, in our CCE-2 method, two P1 centers are considered in a cluster. In this way, we treat both the electron spin and the <sup>14</sup>N nuclear spin on an equal footing and fully consider the anisotropy of the hyperfine tensor for individual JT axes. In addition, we employed the so-called single-sample approach, which treats each bath state independently<sup>39</sup>. We found that our single-sample CCE calculations give a converged  $T_2$  time when averaged over 100 bath states. For an ensemble average, we used 100 different bath spin configurations. We note that in the single-sample CCE method, one can take into account the interaction between clustered bath spins and external spins outside the cluster by adding their Ising-like interaction as a mean-field effect. The single-sample CCE method combined with the mean-field method was shown to produce a robust solution for sparse electron spin baths at the CCE-2 level of theory<sup>54,55</sup>, which we adopted in this study. In Supplementary Note 2, details of our CCE computation and convergence test results are provided.

### Density functional theory calculations

To compute the spin Hamiltonian parameters of a P1 center, we conducted DFT calculations using a plane-wave basis set with an energy cutoff of 85 Ry along with projector-augmented wave (PAW) pseudopotentials (QE PAW v0.3.1 set)<sup>59,60</sup> as implemented in the QUANTUM ESPRESSO code<sup>61</sup>. We employed the Perdew–Burke–Ernzerhof semi-local functional to describe the exchange-correlation potential<sup>62,63</sup>. To simulate the presence of an isolated P1 center in diamond, we used the supercell method. The supercell is oriented in the [111] direction and it contains 1007 atoms. The Brillouin zone is sampled with the  $\Gamma$  point only. We used the GIPAW module of the QE code to compute the hyperfine tensor and the quadrupole moment of a P1 center. The core polarization effects were included in the evaluation of spin densities near the nuclei. Our DFT calculations were in excellent agreement with the experimental results for the hyperfine tensor and the quadrupole moment as described in detail in Supplementary Note 2.

## DATA AVAILABILITY

The data that support the findings of this study are available upon reasonable request to the corresponding author.

## CODE AVAILABILITY

The code that were used in this study are available upon reasonable request to the corresponding author.

Received: 11 March 2022; Accepted: 13 July 2022;

Published online: 12 August 2022

## REFERENCES

1. Yao, N. Y. et al. Scalable architecture for a room temperature solid-state quantum information processor. *Nat. Commun.* **3**, 800 (2012).
2. van der Sar, T. et al. Decoherence-protected quantum gates for a hybrid solid-state spin register. *Nature* **484**, 82–86 (2012).
3. Waldherr, G. et al. Quantum error correction in a solid-state hybrid spin register. *Nature* **506**, 204–207 (2014).
4. Bradley, C. E. et al. A ten-qubit solid-state spin register with quantum memory up to one minute. *Phys. Rev. X* **9**, 031045 (2019).
5. Maze, J. R. et al. Nanoscale magnetic sensing with an individual electronic spin in diamond. *Nature* **455**, 644–647 (2008).
6. Taylor, J. M. et al. High-sensitivity diamond magnetometer with nanoscale resolution. *Nat. Phys.* **4**, 810–816 (2008).
7. Barry, J. F. et al. Sensitivity optimization for NV-diamond magnetometry. *RMP* **92**, 015004 (2020).
8. Mamin, H. J. et al. Nanoscale nuclear magnetic resonance with a nitrogen-vacancy spin sensor. *Science* **339**, 557–560 (2013).
9. Bernien, H. et al. Heralded entanglement between solid-state qubits separated by three metres. *Nature* **497**, 86–90 (2013).
10. Hensen, B. et al. Loophole-free Bell inequality violation using electron spins separated by 1.3 kilometres. *Nature* **526**, 682–686 (2015).
11. Abobeih, M. H. et al. One-second coherence for a single electron spin coupled to a multi-qubit nuclear-spin environment. *Nat. Commun.* **9**, 1–8 (2018).
12. Bar-Gill, N., Pham, L. M., Jarmola, A., Budker, D. & Walsworth, R. L. Solid-state electronic spin coherence time approaching one second. *Nat. Commun.* **4**, 1–6 (2013).
13. Herbschleb, E. et al. Ultra-long coherence times amongst room-temperature solid-state spins. *Nat. Commun.* **10**, 1–6 (2019).
14. Rodgers, L. V. H. et al. Materials challenges for quantum technologies based on color centers in diamond. *MRS Bull.* **46**, 623–633 (2021).
15. Osterkamp, C. et al. Engineering preferentially-aligned nitrogen-vacancy centre ensembles in CVD grown diamond. *Sci. Rep.* **9**, 5786 (2019).
16. Yang, W., Ma, W.-L. & Liu, R.-B. Quantum many-body theory for electron spin decoherence in nanoscale nuclear spin baths. *Rep. Prog. Phys.* **80**, 016001 (2016).
17. Stanwix, P. L. et al. Coherence of nitrogen-vacancy electronic spin ensembles in diamond. *Phys. Rev. B* **82**, 201201 (2010).
18. Balasubramanian, G. et al. Ultralong spin coherence time in isotopically engineered diamond. *Nat. Mater.* **8**, 383–387 (2009).
19. Mizuuchi, N. et al. Coherence of single spins coupled to a nuclear spin bath of varying density. *Phys. Rev. B* **80**, 041201 (2009).
20. Zhao, N., Ho, S.-W. & Liu, R.-B. Decoherence and dynamical decoupling control of nitrogen vacancy center electron spins in nuclear spin baths. *Phys. Rev. B* **85**, 115303 (2012).
21. Wang, Z.-H., de Lange, G., Ristè, D., Hanson, R. & Dobrovitski, V. V. Comparison of dynamical decoupling protocols for a nitrogen-vacancy center in diamond. *Phys. Rev. B* **85**, 155204 (2012).
22. Loubser, J. H. N. & Wyk, J. A. V. Electron spin resonance in the study of diamond. *Rep. Prog. Phys.* **41**, 1201–1248 (1978).
23. Hanson, R., Gywat, O. & Awschalom, D. D. Room-temperature manipulation and decoherence of a single spin in diamond. *Phys. Rev. B* **74**, 161203 (2006).
24. Kennedy, T., Colton, J., Butler, J., Linares, R. & Doering, P. Long coherence times at 300 K for nitrogen-vacancy center spins in diamond grown by chemical vapor deposition. *Appl. Phys. Lett.* **83**, 4190–4192 (2003).
25. Hanson, R., Dobrovitski, V., Feiguin, A., Gywat, O. & Awschalom, D. Coherent dynamics of a single spin interacting with an adjustable spin bath. *Science* **320**, 352–355 (2008).
26. Lange, G. D., Wang, Z. H., Ristè, D., Dobrovitski, V. V. & Hanson, R. Universal dynamical decoupling of a single solid-state spin from a spin bath. *Science* **330**, 60–63 (2010).
27. Takahashi, S., Hanson, R., Van Tol, J., Sherwin, M. S. & Awschalom, D. D. Quenching spin decoherence in diamond through spin bath polarization. *Phys. Rev. Lett.* **101**, 047601 (2008).
28. De Lange, G. et al. Controlling the quantum dynamics of a mesoscopic spin bath in diamond. *Sci. Rep.* **2**, 1–5 (2012).
29. Bauch, E. et al. Decoherence of ensembles of nitrogen-vacancy centers in diamond. *Phys. Rev. B* **102**, 134210 (2020).
30. Li, S. et al. Determination of local defect density in diamond by double electron-electron resonance. *Phys. Rev. B* **104**, 094307 (2021).
31. Stepanov, V. & Takahashi, S. Determination of nitrogen spin concentration in diamond using double electron-electron resonance. *Phys. Rev. B* **94**, 024421 (2016).
32. Bar-Gill, N. et al. Suppression of spin-bath dynamics for improved coherence of multi-spin-qubit systems. *Nat. Commun.* **3**, 858 (2012).
33. Wang, Z.-H. & Takahashi, S. Spin decoherence and electron spin bath noise of a nitrogen-vacancy center in diamond. *Phys. Rev. B* **87**, 115122 (2013).
34. Edmonds, A. M. et al. Characterisation of CVD diamond with high concentrations of nitrogen for magnetic-field sensing applications. *Mater. Quantum Technol.* **1**, 025001 (2021).
35. Tetienne, J.-P. et al. Prospects for nuclear spin hyperpolarization of molecular samples using nitrogen-vacancy centers in diamond. *Phys. Rev. B* **103**, 014434 (2021).
36. Zu, C. et al. Emergent hydrodynamics in a strongly interacting dipolar spin ensemble. *Nature* **597**, 45–50 (2021).
37. Degen, M. J. et al. Entanglement of dark electron-nuclear spin defects in diamond. *Nat. Commun.* **12**, 3470 (2021).
38. Mindarava, Y. et al. Efficient conversion of nitrogen to nitrogen-vacancy centers in diamond particles with high-temperature electron irradiation. *Carbon* **170**, 182–190 (2020).
39. Yang, W. & Liu, R.-B. Quantum many-body theory of qubit decoherence in a finite-size spin bath. *Phys. Rev. B* **78**, 085315 (2008).
40. Yang, W. & Liu, R.-B. Quantum many-body theory of qubit decoherence in a finite-size spin bath. II. Ensemble dynamics. *Phys. Rev. B* **79**, 115320 (2009).
41. Cuijia, K. S., Herb, K., Zopes, J., Abendroth, J. M. & Degen, C. L. Parallel detection and spatial mapping of large nuclear spin clusters. *Nat. Commun.* **13**, 1260 (2022).
42. Pezagna, S., Naydenov, B., Jelezko, F., Wrachtrup, J. & Meijer, J. Creation efficiency of nitrogen-vacancy centres in diamond. *New J. Phys.* **12**, 065017 (2010).
43. Ziem, F., Garsi, M., Fedder, H. & Wrachtrup, J. Quantitative nanoscale MRI with a wide field of view. *Sci. Rep.* **9**, 12166 (2019).
44. Ku, M. J. H. et al. Imaging viscous flow of the Dirac fluid in graphene. *Nature* **583**, 537–541 (2020).
45. Jarmola, A., Acosta, V. M., Jensen, K., Chemerisov, S. & Budker, D. Temperature- and Magnetic-Field-Dependent Longitudinal Spin Relaxation in Nitrogen-Vacancy Ensembles in Diamond. *Phys. Rev. Lett.* **108**, 197601 (2012).
46. Wang, H.-J. et al. Optically detected cross-relaxation spectroscopy of electron spins in diamond. *Nat. Commun.* **5**, 4135 (2014).
47. Bersuker, I. *The Jahn-Teller Effect*. (Cambridge University Press, 2006).
48. Deák, P., Aradi, B., Kaviani, M., Frauenheim, T. & Gali, A. Formation of NV centers in diamond: a theoretical study based on calculated transitions and migration of nitrogen and vacancy related defects. *Phys. Rev. B* **89**, 075203 (2014).
49. Smith, W. V., Sorokin, P. P., Gelles, I. L. & Lasher, G. J. Electron-spin resonance of nitrogen donors in diamond. *Phys. Rev.* **115**, 1546–1552 (1959).
50. Ammerlaan, C. A. J. & Burgemeister, E. A. Reorientation of nitrogen in type-Ib diamond by thermal excitation and tunneling. *Phys. Rev. Lett.* **47**, 954–957 (1981).
51. Witzel, W. M. & Das Sarma, S. Quantum theory for electron spin decoherence induced by nuclear spin dynamics in semiconductor quantum computer architectures: spectral diffusion of localized electron spins in the nuclear solid-state environment. *Phys. Rev. B* **74**, 035322 (2006).
52. Ye, M., Seo, H. & Galli, G. Spin coherence in two-dimensional materials. *Npj Comput. Mater.* **5**, 44 (2019).
53. Seo, H. et al. Quantum decoherence dynamics of divacancy spins in silicon carbide. *Nat. Commun.* **7**, 12935 (2016).
54. Witzel, W. M., Carroll, M. S., Morello, A., Cywiński, Ł. & Das Sarma, S. Electron spin decoherence in isotope-enriched silicon. *Phys. Rev. Lett.* **105**, 187602 (2010).
55. Witzel, W. M., Carroll, M. S., Cywiński, Ł. & Das Sarma, S. Quantum decoherence of the central spin in a sparse system of dipolar coupled spins. *Phys. Rev. B* **86**, 035452 (2012).
56. Reynhardt, E. C., High, G. L. & Wyk, J. A. v. Temperature dependence of spin-spin and spin-lattice relaxation times of paramagnetic nitrogen defects in diamond. *J. Chem. Phys.* **109**, 8471–8477 (1998).
57. Belthangady, C. et al. Dressed-state resonant coupling between bright and dark spins in diamond. *Phys. Rev. Lett.* **110**, 157601 (2013).
58. Pellet-Mary, C., Huillery, P., Perdriat, M., Tallaire, A. & Hétet, G. Optical detection of paramagnetic defects in diamond grown by chemical vapor deposition. *Phys. Rev. B* **103**, L100411 (2021).
59. Blöchl, P. E. Projector augmented-wave method. *Phys. Rev. B* **50**, 17953–17979 (1994).

60. Dal Corso, A. Pseudopotentials periodic table: From H to Pu. *Comput. Mater. Sci.* **95**, 337–350 (2014).
61. Giannozzi, P. et al. QUANTUM ESPRESSO: a modular and open-source software project for quantum simulations of materials. *J. Phys.: Condens. Matter* **21**, 395502 (2009).
62. Hamann, D. R. Optimized norm-conserving Vanderbilt pseudopotentials. *Phys. Rev. B* **88**, 085117 (2013).
63. Schlipf, M. & Gygi, F. Optimization algorithm for the generation of ONCV pseudopotentials. *Comput. Phys. Commun.* **196**, 36–44 (2015).

## ACKNOWLEDGEMENTS

We thank Sang-Yun Lee and Young-wook Cho for the useful discussions. This work was supported by the National Research Foundation of Korea (NRF) grant funded by the Korean government (MSIT) (No. 2018R1C1B6008980, No. 2019M3E4A1078666, No. 2021R1A4A1032085) and by the National Supercomputing Center with supercomputing resources including technical support (KSC-2019-CRE-0156). This research was supported by the Institute of Information and Communications Technology (IITP) Planning & Evaluation grant funded by the Korean government (MSIT) (Grant No. 2019-000296). J.L. and S.H. are supported by the Open Research Program (ORP) from the Korea Institute of Science and Technology. This work was supported by the National Supercomputing Center with supercomputing resources including technical support (KSC-2019-CRE-0156).

## AUTHOR CONTRIBUTIONS

H.P. and J.L. are co-first authors on this work. H.P. developed the CCE code and performed the calculations. H.S., J.L., and S.O. devised the study. H.P., J.L., and H.S. analyzed the results. H.S., S.H. supervised the study. All authors participated in the analysis of the results and paper write-up.

## COMPETING INTERESTS

The authors declare no competing interests.

## ADDITIONAL INFORMATION

**Supplementary information** The online version contains supplementary material available at <https://doi.org/10.1038/s41534-022-00605-4>.

**Correspondence** and requests for materials should be addressed to Sangwon Oh or Hosung Seo.

**Reprints and permission information** is available at <http://www.nature.com/reprints>

**Publisher's note** Springer Nature remains neutral with regard to jurisdictional claims in published maps and institutional affiliations.



**Open Access** This article is licensed under a Creative Commons Attribution 4.0 International License, which permits use, sharing, adaptation, distribution and reproduction in any medium or format, as long as you give appropriate credit to the original author(s) and the source, provide a link to the Creative Commons license, and indicate if changes were made. The images or other third party material in this article are included in the article's Creative Commons license, unless indicated otherwise in a credit line to the material. If material is not included in the article's Creative Commons license and your intended use is not permitted by statutory regulation or exceeds the permitted use, you will need to obtain permission directly from the copyright holder. To view a copy of this license, visit <http://creativecommons.org/licenses/by/4.0/>.

© The Author(s) 2022, corrected publication 2022